

# High energy $\gamma$ -ray detection of supernova remnants in the Large Magellanic Cloud

R. Campana<sup>1</sup>\*, E. Massaro<sup>2</sup>, F. Bocchino<sup>3</sup>, M. Miceli<sup>3,4</sup>, S. Orlando<sup>3</sup>, A. Tramacere<sup>5</sup>

<sup>1</sup> *INAF/OAS, via Gobetti 101, 40129, Bologna, Italy*

<sup>2</sup> *INAF/IAPS, via del Fosso del Cavaliere 100, I-00113 Roma, Italy*

<sup>3</sup> *INAF/Osservatorio Astronomico di Palermo, Piazza del Parlamento 1, I-90134 Palermo, Italy*

<sup>4</sup> *Dipartimento di Fisica e Chimica E. Segrè, Università di Palermo, Piazza del Parlamento 1, 90134, Palermo, Italy*

<sup>5</sup> *Department of Astronomy, University of Geneva, Chemin Pegasi 51, 1290, Versoix, Switzerland*

Accepted 2022 July 1. Received 2022 June 13; in original form 2022 April 22.

## ABSTRACT

We present the results of a cluster search in the  $\gamma$ -ray sky images of the Large Magellanic Cloud (LMC) region by means of the Minimum Spanning Tree (MST) and DBSCAN algorithms, at energies higher than 6 and 10 GeV, using 12 years of *Fermi*-LAT data. Several significant clusters were found, the majority of which associated with previously known  $\gamma$ -ray sources. We confirm our previous detection of the Supernova Remnants N 49B and N 63A and found new significant clusters associated with the SNRs N 49, N 186D and N 44. These sources are among the brightest X-ray remnants in the LMC and corresponds to core-collapse supernovae interacting with dense HII regions, indicating that an hadronic origin of high energy photons is the most likely process.

**Key words:**  $\gamma$ -rays: observations —  $\gamma$ -rays: source detection — Supernova Remnants — Large Magellanic Cloud.

## 1 INTRODUCTION

There is a large consensus in the literature around the hypothesis that Galactic cosmic rays (CRs) may originate at shock fronts of expanding supernova remnants (SNRs) via diffusive shock acceleration of particles (e.g., [Hillas 2005](#) and references therein). According to this scenario, about 10% of the explosion energy of the parent supernova is converted in kinetic energy of accelerated CRs with a broad power law energy spectrum, which extends up to the PeV domain, where the observed spectrum of CRs in our Galaxy is characterized by the “knee”. In the last decades, the SNR paradigm for the origin of CRs was successful in reproducing the main features of their observed intensity, spectrum and chemical composition (e.g., [Ptuskin & Zirakashvili 2005](#)). Furthermore, high energy observations have shown that electrons can be accelerated up to TeV energies ([Koyama et al. 1995](#)) and have allowed to identify the signature of magnetic field amplification ([Bamba et al. 2003](#); [Vink & Laming 2003](#)), an indirect evidence of hadron acceleration at SNR shock fronts ([Bell 2004](#)).

However, despite some undisputable successes of the SNR paradigm in reproducing the observations, some important issues still remain unsolved.  $\gamma$ -ray observations provided evidence of accelerated hadrons up to multi-GeV energies at SNR shocks (e.g., [Ackermann et al. 2013a](#)) but, to date, there is no convincing observational support for the acceleration of hadrons to PeV energies. It is even questioned whether SNRs can accelerate hadrons to PeV energies: the observed expansion rate of some historical young SNRs (Cassiopeia A, Tycho and Kepler) is too low to allow the acceleration of CRs to the energy domain of the knee ([Bell et al. 2013](#)).

To shed some light on the above issues, we need to analyze carefully the spectrum of Galactic CRs above GeV energies and to provide physical insight on the origin of the features observed. Thus,  $\gamma$ -ray observations of SNRs are the most natural tool to challenge the SNR paradigm and obtain observational evidence in favour or against this scenario ([Gabici 2017](#)). A first important step is to enlarge the sample of  $\gamma$ -ray sources associated with SNRs in order to improve the statistics of possible CRs accelerators.

The Large Magellanic Cloud (LMC) is a nearby small galaxy rich of young astronomical objects and Supernova Remnants (SNR). It was proposed as an interesting target in the early period of  $\gamma$ -ray astronomy by [Ginzburg \(1972\)](#), subsequently developed by [Ginzburg & Ptuskin \(1984\)](#), for testing the metagalactic origin of cosmic rays via the  $\pi^0$  decay process. The discovery of the emission from LMC at energies higher than 100 MeV was reported by [Sreekumar et al. \(1992\)](#), on the basis of EGRET-CGRO observations, who evaluated that the cosmic rays in the LMC have a density comparable to the ones in our Galaxy. Several compact high energy sources were found in the LMC, since the discovery on 1979 March 5 of the first magnetar SGR 0526–66 ([Mazets et al. 1979a,b](#)) later associated with the SNR N 49 ([Cline et al. 1982](#)). [Abdo et al. \(2010\)](#) reported a first study of the LMC region based on the 11-month *Fermi*-Large Area Telescope (LAT) observations and revealed the massive star forming region 30 Doradus as a bright high energy source. [Ackermann et al. \(2016\)](#) performed the first detailed analysis of the LMC region considering a much richer *Fermi*-LAT data spanning the first 6 years of the mission and detected four sources. In the last version (DR2) of the 4FGL catalogue released by the *Fermi*-LAT collaboration ([Abdollahi et al. 2020](#); [Ballet et al. 2020](#)) in the LMC region there are 18 sources, detected in the 50 MeV – 1 TeV energy range, of which 4 are reported

\* E-mail: [riccardo.campana@inaf.it](mailto:riccardo.campana@inaf.it)

as extended features and 7 are present also in the 3FHL catalogue (Ajello et al. 2017). Furthermore, possible background extragalactic counterparts (unclassified blazar or BL Lac objects) are indicated for 9 of these 4FGL sources.

At TeV energies, the H.E.S.S. collaboration observed three sources up to about 10 TeV in the LMC (H.E.S.S. Collaboration et al. 2015), two of them associated with the SNRs N 157B (H.E.S.S. Collaboration et al. 2012) and N 132D, the former containing the highest known spin-down luminosity pulsar PSR J0537–6910 (Marshall et al. 1998a; Cusumano et al. 1998) with the fast period of 16 ms.

Campana et al. (2018a), hereafter Paper I, used the data collected by the *Fermi*-LAT telescope (Ackermann et al. 2012) in 9 years of operation for a cluster search at energies higher than 10 GeV, and reported the discovery of high energy emission from the two SNRs N 49B and N 63A. In the present paper we extend this analysis of the LMC region using a richer data set of 12 years of *Fermi*-LAT observation. As in Paper I we applied the Minimum Spanning Tree (hereafter MST, Campana et al. 2008, 2013) source-detection method for extracting photon clusters likely corresponding to genuine  $\gamma$ -ray sources, as already successfully applied in a series of papers (Bernieri et al. 2013; Campana et al. 2015, 2016a,b,c, 2017, 2018b; Campana & Massaro 2021). Furthermore, the analysis was verified by an independent cluster search using the DBSCAN algorithm (Tramacere & Vecchio 2013).

The results of this new analysis confirm the previous SNR detections with a higher significance, and found some other photon clusters at positions very close to those of SNRs not previously associated with  $\gamma$ -ray emitters.

The outline of this paper is as follows. In Section 2 the data selection and the MST and DBSCAN algorithms are described, while the analysis of the LMC region is presented in Section 3. In Section 4 we deepen the analysis of some interesting SNR counterparts to MST clusters, while in Section 5 the results are summarized.

## 2 PHOTON SELECTION AND CLUSTER ANALYSIS OF LMC HIGH ENERGY $\gamma$ -RAY DATA

### 2.1 Data selection in the LMC region

The full *Fermi*-LAT dataset, including events above 3 GeV in the 12 years from 2008 August 4 to 2020 August 4, and processed with the Pass 8, release 3, reconstruction algorithm and responses, was downloaded in the form of weekly files from the FSSC archive<sup>1</sup>. The event lists were then filtered applying the standard selection criteria on data quality and zenith angle (source class events, `evclass` 128), front and back converting (`evtype` 3), up to a maximum zenith angle of  $90^\circ$ . Events were then screened for standard good time interval selection. Then, a region  $12^\circ \times 9^\circ$ , in Galactic coordinates  $273^\circ < l < 285^\circ$  and  $-38^\circ < b < -29^\circ$  and approximately centred at the LMC, was selected and the MST algorithm was applied. Figure 1 shows the photon maps in this region at energies higher than 6 GeV (upper panel) and higher than 10 GeV (lower panel).

The general structure of the  $\gamma$ -ray emission in the LMC region is very complex. The last DR2 release of the 4FGL catalogue reports several sources as extended and only 6 of them are at Galactic latitude higher than  $20^\circ$ : four are in the LMC, one in the Small Magellanic Cloud (SMC) and the last one in the Fornax A region.

One of the extended features, 4FGL J0519.9–6845e, has a radius of  $3^\circ$  and therefore it covers the entire central region of LMC including

the very bright complex of 30 Dor and about 75% of the known SNRs, while the other three have smaller radii and are in localised bright regions inside the largest one. In Figure 1 these regions are plotted as large magenta circles. The same catalogue reports 13 more point sources within the considered regions: 5 are in the circle of the largest one while 8 are outside this boundary, and the latter ones have possible associations with confirmed or candidate blazars.

Given such conditions of a high local diffuse emission, the sorting of point-like sources is a quite difficult work, and particular approaches should be adopted. Our basic choice is to search clusters at energies higher than 10 GeV, since the diffuse component is rather weak in this band. Once a list of clusters is obtained, we searched for correspondent features at lower energies and, if they were found, the cluster was considered to be confirmed. However, in these analyses we had to use smaller fields not including the 30 Dor nebula, because its relatively high number of photons produces a too short mean angular separation in the field for a safe cluster search. In these analyses at lower energies the resulting cluster parameters were generally much lower than above 6 GeV, and the extraction of clusters was less stable: in particular, small changes in the selection parameters could give different structures.

The LMC is particularly rich of SNRs. The work of Maggi et al. (2016) reports 59 remnants. A richer catalogue, which includes the previous one, adding another group of 15 SNR candidates, is provided by Bozzetto et al. (2017); a further sample of 19 optically selected SNR candidates is given by Yew et al. (2021). As it will be clear from the results of this work, we did not find any well established positional correspondence between clusters and the Yew et al. (2021) sources and the Bozzetto et al. (2017) candidate sources, and therefore we will limit our analysis to the Maggi et al. (2016) sample, which contains the brightest and genuine SNRs.

### 2.2 Description of photon cluster detection algorithms

#### 2.2.1 Minimum Spanning Tree

The MST (see, for instance, Cormen et al. 2009 and also Campana et al. 2008, 2013) is a topometric tool that can be used for searching spatial concentrations in a field of points. The application of this method to the  $\gamma$ -ray sky and detailed descriptions of its theoretical principles and selection criteria were presented elsewhere (e.g., in Campana et al. 2018a). As a consequence, we summarize here only the properties the main parameters used for the cluster selection.

In a two-dimensional set of  $N_n$  points (*nodes*), one can construct the unique *tree* (a graph without closed loops) which connects all the nodes with the minimum total weight,  $\min[\sum_i \lambda_i]$ , where the elements of the set  $\{\lambda\}$  are, in this case, the angular distances between photon arrival directions.

The *primary* cluster selection is then performed in two following steps: *i) separation*, the removal of all the edges having a length  $\lambda \geq \Lambda_{\text{cut}}$ , usually defined in units of the mean edge length  $\Lambda_m = (\sum_i \lambda_i)/N_n$  in the MST; *ii) elimination*: removal of all the sub-trees having a number of nodes  $N \leq N_{\text{cut}}$ . This leaves only the clusters with a number of photons higher than this threshold. In this paper we adopt the simplifying notation  $\Lambda_{\text{cut}} = 0.6$ , implying the factor  $\Lambda_m$ . A successive *secondary* selection is applied for extracting the most robust candidates for  $\gamma$ -ray sources. The most important parameter here is the cluster *magnitude*:

$$M_k = N_k g_k \quad (1)$$

where  $N_k$  is the number of nodes in the cluster  $k$  and the *clustering parameter*  $g_k$  is the ratio between  $\Lambda_m$  and  $\lambda_{m,k}$ , the mean length

<sup>1</sup> <http://fermi.gsfc.nasa.gov/ssc/data/access/>

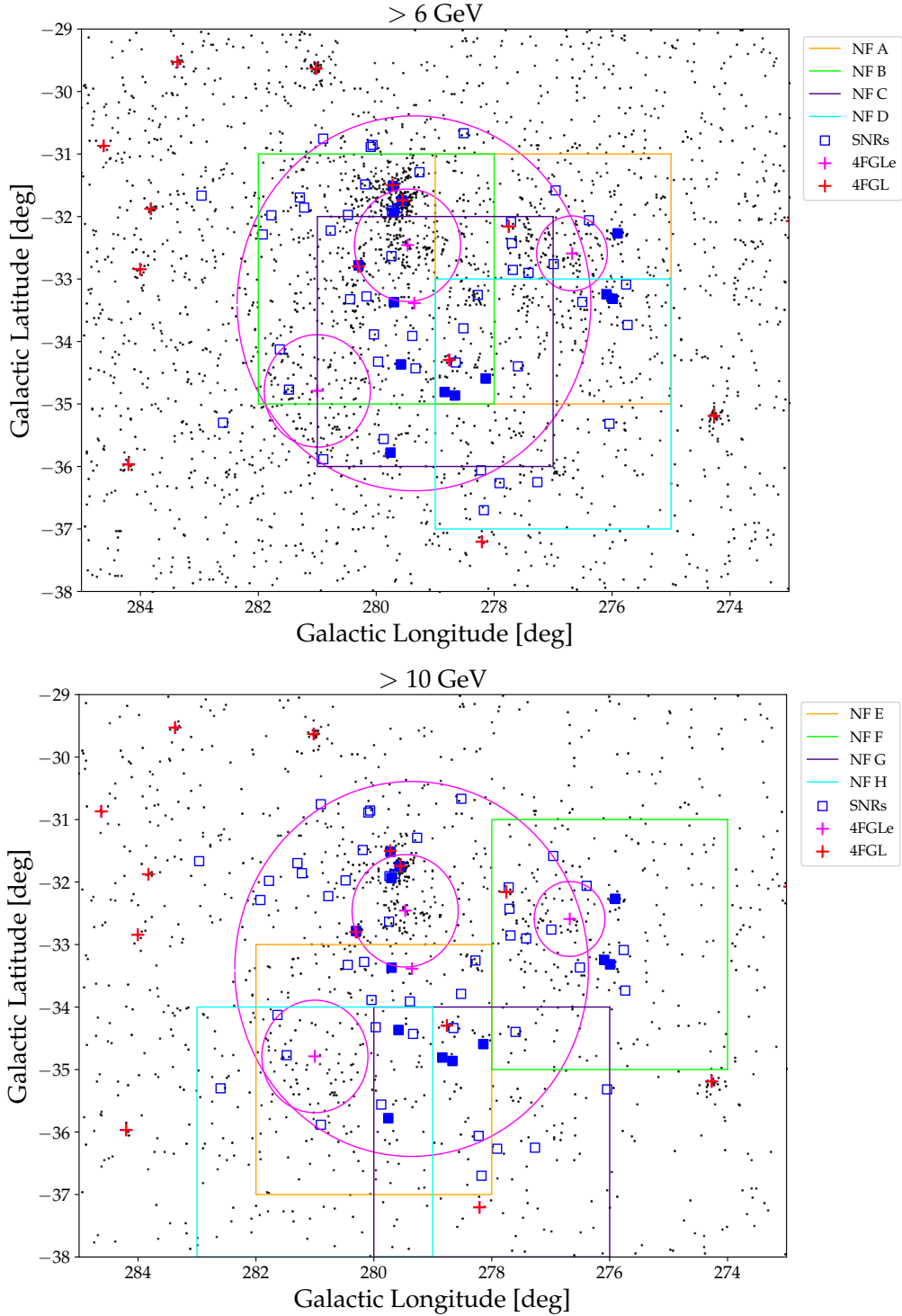


**Figure 1.** Photon maps in equatorial coordinates of the sky region ( $12^\circ \times 9^\circ$  in a Galactic coordinate frame) centered at the LMC, at energies higher than 6 GeV (upper panel) and higher than 10 GeV (lower panel). Black points in each panel are the photons. Magenta circles (centred at the magenta crosses) circles correspond to the sizes of the extended 4FGL-DR2 sources, while red crosses mark the other 4FGL sources. Blue squares are the SNRs in the [Maggi et al. \(2016\)](#) catalogue: those marked by a filled square have with a X-ray luminosity higher than  $10^{36}$  erg/s. Large square regions, shown for clarity's sake split in the two panels, mark the narrow fields (NF) considered in our analysis: note that only NF B in the upper panel includes the bright 30 Doradus complex.

over the  $k$ -th cluster edges. Campana et al. (2013) found that  $\sqrt{M}$  is well correlated with other statistical source significance parameters, in particular with Test Significance from the Maximum Likelihood (Mattox et al. 1996) analysis. A lower threshold value of  $M$  around 15–20 would reject the large majority of spurious low-significance clusters.

The centroid coordinates are computed by means of a weighted mean of the cluster photon arrival directions (see Campana et al. 2013). The radius of the circle centred at the centroid and containing the 50% of photons in the cluster, the *median radius*  $R_m$ , for a genuine point-like  $\gamma$ -ray source should be smaller than or comparable to the 68% containment radius of instrumental Point Spread Function (PSF). This radius varies from  $0^\circ.2$  at 3 GeV to  $0^\circ.14$  at 10 GeV in the case of a bright source for diffuse class front-observed events (Ackermann et al. 2013b). It is also expected that the angular distance between the cluster centroid and a possible counterpart would be lower than the latter value. We also define the *maximum radius*  $R_{\max}$  as the distance between the centroid and the farthest photon in the cluster, usually of some arcminutes for a point-like source and a few tens of arcminutes either for extended structures or for unresolved close pairs of sources.

In the present analysis we adopted the following criteria for the secondary selection. For clusters having a number of photons  $N > 5$ , a threshold of  $M \geq 20$  was adopted, while for clusters having  $N = 4$  and  $N = 5$  nodes, a threshold of  $g \geq 3.5$  and  $g \geq 3.0$  (corresponding to  $M \geq 14$  and  $M \geq 15$ , respectively) was chosen in order to extract only structures with a photon density much higher than the surrounding and reduce in this way the probability for random clustering, as suggested by numerical simulations (Campana et al. 2013). We also extended our analysis to low significance clusters ( $M < 20$ ), because of the possible associations either with extended features, or with faint sources, as verified by *a posteriori* comparisons with literature data sets. According to Campana et al. (2013) we expect that a percentage of around 50% of these low significance and “poor” clusters could be spurious and therefore those expected to be associated with an interesting counterparts must be validated by further analysis.

### 2.2.2 Narrow Field analysis

We verified the stability of these clusters performing some further targeted searches in several suitably selected narrow fields, hereafter NF. The use of these smaller-sized fields implies a variation of the mean angular separation between photons because of the different occurrence of high photon density regions. We considered eight  $4^\circ \times 4^\circ$  fields selected for including some subsample of detected clusters, shown in Figure 1, where the fields are identified by a letter from A to H. These fields were generally selected to exclude the bright complex of 30 Dor, with the only exception of NF B, and partially NF C, and therefore they are useful for detecting clusters not very rich and dense. The lower values of the considered energy intervals were 6, 8, 10 and 12 GeV. A cluster is therefore considered *very stable* (VS) when it is found with high  $M$  values in all narrow field searches, *stable* (S) when it results with a low  $M$  only in some selections, and *poorly stable* (PS) when it appears only in a small number of fields generally with a low  $M$ .

### 2.2.3 DBSCAN

The *Density Based Spatial Clustering of Applications with Noise* algorithm (DBSCAN, Easter et al. 1996), is a topometric density-based clustering method, that uses local density of points to find

clusters in data sets that are affected by background noise. Thanks to its embedded capability to distinguish background noise (even when the background is not uniform), it has been successfully used to detect sources in  $\gamma$ -ray photon lists Tramacere & Vecchio (2013) and in CCD optical images Tramacere et al. (2016). For a detailed description we refer to Tramacere & Vecchio (2013), and in the following we give only a brief description of the method and its application.

Let  $S$  be a set of photons, where each element is described by the sky coordinates. The distance between two given elements ( $p_l, p_k$ ) is defined as the angular distance on the unit sphere,  $\rho(p_l, p_k)$ . Let  $N_\varepsilon(p_i)$  be the set of points contained within a radius  $\varepsilon$ , centred on  $p_i$ , and  $|N_\varepsilon(p_i)|$  the number of contained points, i.e., the estimator of the local density, and  $K$  a threshold value. Clusters are built according to the local density around each point  $p_i$ . A point is classified according to the local density defined as:

- *core point*: if  $|N_\varepsilon(p_i)| \geq K$ .
- *border point*: if  $|N_\varepsilon(p_i)| < K$ , but at least one core point belongs to  $N_\varepsilon(p_i)$ .
- *noise point*, if both the conditions above are not satisfied.

Points are classified according to their inter-connection as:

- *directly density reachable*: a point  $p_j$  is defined *density reachable* from a point  $p_k$ , if  $p_j \in N_\varepsilon(p_k)$  and  $p_k$  is a *core point*.
- *density reachable*: a point  $p_j$  is defined *density reachable* from a point  $p_k$ , if exists a chain of *directly density reachable* points connecting,  $p_j$  to  $p_k$ .
- *density connected*: two points  $p_j, p_k$  are defined *density connected* if exists a *core point*  $p_l$  such that both  $p_j$  and  $p_k$ , are *density reachable* from  $p_l$ .

The DBSCAN builds the cluster by recursively connecting *density connected* points to each set of *core points* found in the set. Each cluster  $C_m$  will be described by the position of the centroid ( $x_c, y_c$ ), the ellipse of the cluster containment, the number of photons in the cluster ( $N_p$ ), and the significance. The ellipse of the cluster containment is defined by major and minor semi-axis ( $\sigma_x$  and  $\sigma_y$ ) and the inclination angle ( $\sigma_\alpha$ ) of the major semi-axis w.r.t. the latitudinal coordinate ( $b$  or  $DEC$ ). The ellipse is evaluated using the principal component analysis method (PCA, Jolliffe 1986).

The detection algorithm proceeds as follows:

- (i) The initial data set is pre-processed, selecting all the photons within an extraction radius ( $R_{\text{extr}}$ ), and above a given threshold energy  $E_{\text{th}}$ .
- (ii) The scanning radius of the DBSCAN  $\varepsilon$  is set equal to the *Fermi-LAT* PSF at  $E_{\text{th}}$ .
- (iii) The background level,  $K_{\text{bkg}}$ , is heuristically estimated as described in the following, and the final cluster list  $C$  is produced performing a DBSCAN run with  $K = K_{\text{bkg}}$  and  $\varepsilon = \text{PSF}(E_{\text{th}})$

The background estimation algorithm proceeds as follows:

- (i) In a first step,  $K$  is estimated from the average photon density within  $R_{\text{extr}}$ , i.e.  $K_{\text{ave}} = \frac{N_{\text{tot}}\Omega_\varepsilon}{\Omega_{R_{\text{extr}}}}$ , where  $\Omega_{R_{\text{extr}}}$  is the angular size of the extraction region,  $\Omega_\varepsilon$  is the angular size of the scanning brush, and  $N_{\text{tot}}$  is the total number of photons within the extraction region.
- (ii) A first run of the DBSCAN is performed with  $K = K_{\text{ave}} + K_{\text{frac}}\sqrt{K_{\text{ave}}}$ , producing a cluster list  $C^*$ .
- (iii) All the photons belonging to the detected clusters are flagged as signal events, and the remaining as background events. The final value of background density,  $K_{\text{bkg}}$ , is evaluated as the average value

of background photons within each circular region centred on each background photon, within a distance equal to  $\varepsilon$ .

(iv) The final detection is performed by setting  $K = K_{\text{bkg}} + K_{\text{frac}}\sqrt{K_{\text{bkg}}}$ .

The significance of a cluster ( $S_{\text{cls}}$ ), evaluated according to the signal-to-noise Likelihood Ratio Test (LRT) method proposed by Li & Ma (1983), and explained in detail in Tramacere & Vecchio (2013), is defined as:

$$S_{\text{cls}} = \sqrt{2 \left( N_{\text{src}}^{\text{in}} \ln \left[ \frac{2N_{\text{src}}^{\text{in}}}{N_{\text{src}}^{\text{in}} + N_{\text{bkg}}^{\text{eff}}} \right] + N_{\text{bkg}}^{\text{eff}} \ln \left[ \frac{2N_{\text{src}}^{\text{in}}}{N_{\text{src}}^{\text{in}} + N_{\text{bkg}}^{\text{eff}}} \right] \right)}. \quad (2)$$

where  $N_{\text{src}}^{\text{in}}$  represents the number of points in each cluster, and  $N_{\text{bkg}}^{\text{eff}}$  is the expected number of background photons within the circle enclosing the most distant cluster point, according to the estimated value of  $N_{\text{bkg}}$ . Assuming that a cluster is due to a background fluctuation, the variable  $S_{\text{cls}}^2$  is expected to follow a chi square distribution, with one degree of freedom ( $\chi(1)^2$ ), hence it defines our test statistics (TS). The value of  $S_{\text{cls}}^2$  is highly correlated with the  $\sqrt{TS}_{\text{LAT}}$  returned by the *Fermi*-LAT analysis (using the same value of  $E_{\text{th}}$ ) with:  $S_{\text{cls}} \approx 0.5\sqrt{TS}_{\text{LAT}}$  (Tramacere & Vecchio 2013).

### 3 CLUSTER SEARCH RESULTS

The high energy image of the LMC is extremely complex and the extraction of individual sources is not a simple process. A first analysis of this region was presented by Ackermann et al. (2016) who investigated the *Fermi*-LAT data obtained in the first six years of observation. Their maps show a large extended region with a dominant maximum in the region of 30 Dor. These authors detected four sources, labelled from P1 to P4: P1 was undoubtedly identified with the pulsar PSR J0540–6919 because of his periodic signal, P2 was found coincident with PSR J0537–6910 and the SNR N 157B, P4 with the SNR N 132D, while P3 was unassociated and after was identified with the first extragalactic  $\gamma$ -ray binary within the SNR DEM L241 (Corbet et al. 2016). Tang (2018) found a new source in the LMC region at energies lower than 10 GeV, which was confirmed by MST (see Paper I) search after extending the energy range down to 7 GeV. The most relevant result in Paper I was the discovery of two significant clusters associated with the two SNRs N 49B and N 63A, that increased to four the number this type of sources in LMC.

On this basis one can reasonably expect that the increase of data would confirm these results and provide more evidence for new SNRs. We therefore applied cluster search to the photon maps at energies above 10 GeV and 6 GeV and extracted clusters with a magnitude  $M \geq 20$ , a value high enough to guarantee a high confidence level as also recently verified by Campana & Massaro (2021). The search was then extended to narrow fields for confirming the clusters detected in the previous steps and, eventually, for sorting new source candidates.

Centroid coordinates and other interesting parameters of the high significance ( $M \geq 20$ ) clusters selected at energies higher than 10 GeV applying MST with  $\Lambda_{\text{cut}} = 0.6$  are reported in the first part of Table 1, while in the second part lists the clusters found at energies above 6 GeV applying  $\Lambda_{\text{cut}} = 0.7$ . In the former part there are 13 clusters, six of which have a positional correspondence with sources in the 4FGL-DR2 catalogue (Abdollahi et al. 2020; Ballet et al. 2020) and with three of the sources found by Ackermann et al. (2016), which are indicated by P1, P2 and P4, while P3 was not detected. All clusters reported in Paper I are confirmed, although the

centroid coordinates of extended clusters do not match precisely but are within their maximum radii. In particular, the two SNRs N 49B and N 63A are now found with a safe  $M$  value and there is a good evidence for high energy emission from some other remnants. A map of the region with the positions of SNRs, 4FGL-DR2 sources and our clusters is given in Figure 2. Finally, we note that no cluster was found at a position near to that of the unassociated P3 source reported by Ackermann et al. (2016): this could be explained by its steep spectrum (the reported spectral index is  $2.8 \pm 0.1$ ) implying a low photon number above 6 GeV.

In the latter part of the Table 1 are reported 17 clusters found in the analysis at energies higher than 6 GeV: essentially all clusters found at higher energies are confirmed, with a couple of uncertain associations as reported in the individual descriptions (see below).

In the following subsections we describe some of the main properties of individual clusters and their possible counterparts.

The results of the parallel DBSCAN analysis are reported in Table 2. The detection has been performed selecting photons above 10 GeV, end cutting a circular region with a radius of  $5^\circ$  around the centre of the same region used for the MST analysis. The value of  $K_{\text{frac}}$  has been set to 3.5, and  $\varepsilon$  has been set equal to  $0^\circ.1$ , close to the *Fermi*-LAT PSF at 10 GeV. We notice an excellent agreement both in the cluster detection and in the photon number implying very close centroid positions. All the MST clusters have a one-to-one match with those detected by the DBSCAN, with the exception of the cluster MST(81.700, –69.129). For this source, the MST has detected a cluster with 17 photons, whilst the DBSCAN has detected two clusters (DBS(81.679, –69.000) and DBS(81.694, –69.235)), with 8 and 7 photons respectively, with a distance of approximately  $7'$ .

#### 3.1 Details on MST clusters at energies > 10 GeV

**MST(77.440, –64.308).** A high significance cluster with a centroid very close to the present one was reported in Paper I. NF analysis confirmed a rich cluster. It is very likely associated with a 4FGL source and the proposed counterpart is a radio and X-ray source, likely a background blazar.

**MST(80.630, –67.891).** This cluster is a new detection and its position is close to that of the SNR N 44, that is at an angular distance from the centroid less than  $4'$ , fully compatible with the  $\gamma$ -ray positional accuracy. This cluster is found in all five NFs where it is included with a value of  $M$  ranging from 17.5 to 30.4, with the only exception of NF B which however includes 30 Dor and has a mean photon separation much lower than the other NFs.

**MST(81.284, –69.618).** It is positionally associated with the source P4 of Ackermann et al. (2016) that is also reported in the 4FGL-DR2. It is only found in NF B and C, with associated clusters having  $M$  equal to 34.5 and 43.3. It was already reported in Paper I and corresponds to the SNR N 132D.

**MST(81.379, –65.928) and MST(81.515, –66.093).** MST analysis found a close pair of clusters: one of them with the centroid nearly coincident with a previously reported feature in Paper I that was associated with the SNR N 49B, while the centroid of the other cluster is very close to the near SNR N 49, at an angular distance of only  $6'66$ , comparable to the typical size of clusters. In Paper I it is reported only a cluster whose association with N 49B was more robust with respect to the one with N 49.

The present analysis with the usual separation length gives two

**Table 1.** Coordinates and main properties of MST clusters with  $M \geq 20$  detected in the LMC sky region at energies higher than 10 GeV (1st section) and higher than 6 GeV (2nd section).  $\Lambda_{\text{cut}}$  values are reported in the first line of each part. Celestial coordinates are J2000, angular distances  $\Delta\theta$  are computed between the centroids of MST clusters and those of indicated counterparts. The letter “e” indicates likely extended structures, see main text for details. Clusters not included in NFs are marked by a dash.

RA °	Dec °	$l$ °	$b$ °	$N$	$g$	$M$	$R_m$ ′	$R_{\text{max}}$ ′	$\Delta\theta$ ′	Stability	Possible counterparts
$E > 10 \text{ GeV}, \Lambda_{\text{cut}} = 0^\circ.6 = 5'5$											
77.440	−64.308	274.297	−35.206	21	3.739	78.517	3.8	13.9	1.65	–	4FGL J0509.9–6417
80.630	−67.891	278.293	−33.311	8	2.782	22.259	4.8	8.9	3.45	VS	N 44
81.284	−69.618	280.275	−32.780	16	3.446	55.132	4.1	15.3	1.96	VS	4FGL J0524.8–6938, P4
									1.35		N 132D
81.379	−65.928	275.919	−33.316	6	3.862	23.175	2.8	7.7	3.66	S	N 49B
81.515	−66.093	276.106	−33.239	9	2.372	21.345	5.4	8.2	0.77	S	N 49
81.700	−69.129	279.672	−32.719	17	2.833	48.161	8.4	13.9	6.28	PS	SNR B0528–692 ?
82.443	−68.704	279.124	−32.521	8	3.514	28.110	3.7	5.7	17.82	VS	4FGL J0530.0–6900e
82.714	−69.199	279.688	−32.352	11	3.419	37.610	4.9	7.0	12.80	VS	4FGL J0530.0–6900e
83.939	−69.490	279.957	−31.884	10	2.813	28.133	5.7	11.1		PS	
83.955	−66.051	275.923	−32.261	12	3.161	37.933	4.6	8.1	0.94	VS	N 63A
e 84.278	−69.160	279.554	−31.806	77	4.803	369.868	7.8	24.8	3.80	VS	4FGL J0537.8–6909, P2
									3.60		N 157B
85.186	−69.329	279.707	−31.467	15	2.924	43.860	5.2	13.7	2.15	S	4FGL J0540.3–6920, P1
									2.99		PSR J0540–6919
									2.98		SNR B0540–693
90.281	−70.568	280.996	−29.636	19	5.449	103.534	2.6	9.2	2.08	–	5BZQ J0601–7036
$E > 6 \text{ GeV}, \Lambda_{\text{cut}} = 0^\circ.7 = 4'5$											
74.306	−66.225	276.949	−36.071	11	2.145	23.600	4.4	11.1	1.25	VS	1WGA J0457.1–6612
74.875	−70.169	281.536	−34.794	7	3.142	21.994	1.9	6.4	3.10	VS	N 186D
77.506	−64.303	274.285	−35.179	31	3.021	93.653	4.6	18.8	0.96	–	4FGL J0509.9–6417
77.934	−68.137	278.817	−34.254	9	2.447	22.019	5.3	7.6	3.73	VS	4FGL J0511.4–6804
									2.37		PMN J0511–6806 bcu
78.936	−72.681	284.028	−32.871	11	2.056	22.615	5.0	9.9	2.05	–	4FGL J0516.1–7240
											PKS 0517–726 bcu
80.627	−67.933	278.344	−33.305	18	2.102	37.830	5.9	11.0	4.49	VS	N 44
81.199	−69.666	280.337	−32.801	22	2.670	58.732	6.2	16.9	1.54	VS	4FGL J0524.8–6938 P4
									2.11		N 132D
81.427	−65.992	275.992	−33.288	17	2.450	41.646	4.6	11.8	5.68/1.80	VS	N 49/N 49B
81.691	−69.016	279.540	−32.740	13	2.176	28.285	5.0	9.7		S	
82.317	−72.740	283.834	−31.878	9	2.858	25.722	2.9	5.9	0.49	–	4FGL J0529.3–7243
											PKS 0530–727 bcu
82.439	−68.993	279.464	−32.479	8	2.575	20.601	3.3	7.4	1.36	S	4FGL J0530.0–6900e
82.477	−68.715	279.135	−32.507	9	3.657	32.917	2.1	4.9		VS	
82.731	−69.217	279.708	−32.343	19	2.601	49.413	5.4	10.9		VS	
83.643	−67.326	277.438	−32.253	15	2.505	37.582	5.5	14.7		PS	
83.951	−66.115	275.998	−32.256	21	2.575	54.075	5.7	12.4	4.68	VS	N 63A
e 84.457	−69.215	279.609	−31.737	216	3.405	735.446	14.3	38.3	3.02	VS	4FGL J0537.8–6909, P2
									3.60		N 157B
90.276	−70.583	281.013	−29.637	38	4.885	185.637	3.4	13.2	1.24	–	5BZQ J0601–7036

nearby clusters: one is very close to N 49 with the magnetar SGR 0526–66, while the other is closer to N 49B at a distance of  $\sim 3'.7$ , compatible with the cluster size. Searches with a higher separation cluster (0.8) give a unique joint cluster with a photon number around 16 and  $M \approx 40$ . A cluster appears also in the NF searches with a position intermediate between the two remnants.

A  $2^\circ \times 2^\circ$  size photon map of the region is shown in Figure 3, where the clusters and SNRs positions are given together with the 4FGL-DR2 sources and 12Y-MST clusters. Note that the pair N 49 and N 49B is unresolved in this catalogue, while the source 4FGL J0531.8–6639e is classified as extended and without any reported possible counterpart; there is an entry in the MST large field analysis for the 12Y-MST catalogue close to its position but the parameters

are just below the adopted selection thresholds. It should be emphasised that with the present analysis no definite statement about the separation of these two features can be given, since the occurrence of only one more photon in the intermediate position might be sufficient to join the two structures in a single cluster. However, when considering a single connected cluster it appears clearly elongated in the direction connecting the two SNRs, suggesting that photons are likely originated by both objects.

The analysis in NF A above 10 GeV with  $\Lambda_{\text{cut}} = 0.6$  found only 4 clusters with  $M > 17$ , two of which corresponding to the ones in the complete field, while in the energy band higher than 6 GeV only an unresolved feature with  $M = 28.4$  is found, likely due to the broader PSF.

**Table 2.** Clusters found in a DBSCAN analysis of the same LMC field. Cluster coordinates, number of events, significance according to Eq. 2 and cluster radius are reported. Moreover, association with known sources and/or MST clusters reported in Table 1, with the value of the relative spatial separation. The two clusters DBS(81.679,  $-69.000$ ) and DBS(81.694,  $-69.235$ ) are a possible fragmentation of the cluster MST(81.700,  $-69.129$ ).

RA °	DEC °	L °	B °	$N_{\text{evt}}$	$S_{\text{cls}}$	$R_{\text{cl}}$ '	Association	MST $\Delta\theta$ '
77.456	-64.289	274.273	-35.203	19	3.58	5.52	4FGL J0509.9-6417	1.18
80.738	-67.932	278.334	-33.264	8	1.45	6.10	N 44	3.53
81.292	-69.614	280.269	-32.778	14	2.86	5.39	N 132D	0.32
81.305	-65.934	275.930	-33.345	7	1.73	5.00	N 49B	1.85
81.519	-66.116	276.132	-33.235	6	1.72	5.06	N 49	1.34
81.679	-69.000	279.522	-32.747	8	1.96	5.22	*MST(81.700, $-69.129$ )	7.6
81.694	-69.235	279.797	-32.704	7	1.82	4.64	*MST(81.700, $-69.129$ )	6.4
82.429	-68.740	279.167	-32.521	10	2.05	5.93	4FGLe	2.17
82.702	-69.197	279.686	-32.356	11	2.39	5.51	4FGLe	0.27
83.797	-69.479	279.951	-31.934	6	1.40	5.08	—	3.02
83.968	-66.047	275.917	-32.256	12	2.25	6.10	N 63A	0.43
84.324	-69.157	279.548	-31.790	76	7.13	9.98	N 157B	1.00
85.124	-69.346	279.730	-31.487	10	2.39	5.53	PSR B0540-69	1.67
90.289	-70.576	281.007	-29.633	19	4.02	4.20	5BZQ J0601-7036	0.58

**MST(81.700,  $-69.129$ ).** A cluster near this position is reported in Paper I only for  $\Lambda_{\text{cut}} = 0.5$ , but in the present search it is found at the two cut distances employed, with different photon numbers and  $R_{\text{max}}$  values. It is located near the centre of the extended source 4FGL-DR2 J0530.0-6900e which contains 30 Dor and N 157B, and therefore with a high local photon density. It is close to SNR B0528-692, but the separation is higher than  $6'$ , however the median radius is over this distance; the analysis with  $\Lambda_{\text{cut}} = 0.5$  gives a cluster of only 6 photons and the distance to the remnants is slightly lower than  $R_{\text{max}}$ . NF B and C searches do not confirm a stable cluster and give a marginally significant feature in the extended 4FGL-DR2 source. This association shall be considered uncertain.

**MST(82.443,  $-68.704$ ) and MST(82.714,  $-69.199$ ).** These two nearby rather compact clusters are located at about  $11'$  and  $18'$  from the centre of the same 4FGL-DR2 extended source as the previous one. No known SNR is close enough to their centroids to be associated with, however, there is a long list of stars and other sources within a distance of  $3'$ , and the selection of a reliable counterpart candidate is a very difficult task. NF analysis is in agreement with this result and therefore one cannot exclude that the extended feature is due to some close unresolved structures.

**MST(83.939,  $-69.490$ ).** This is a quite peculiar cluster because it is found with  $\Lambda_{\text{cut}} = 0.6$ , but not with a lower value. The clustering factor is rather low, but not enough to produce a magnitude below the threshold. For  $\Lambda_{\text{cut}} = 0.7$  a cluster of 20 photons and a very close position is sorted but with a lower  $g$  and  $R_{\text{max}} = 23.5'$ ; for  $\Lambda_{\text{cut}} = 0.8$  it is merged in a single and very large feature with  $R_{\text{max}} \approx 1^\circ$  and is connected to the large 30 Dor nebula. We did not find a good candidate for a possible counterpart. Note that the cluster is a region containing some SNRs: at an angular separation of  $13.3'$  there is the very young remnant of SN 1987a, the bright source N 157B is at  $21.7'$ , and the two other remnants B0540-693 and B0534-699 are at  $25.2'$  and  $27.2'$ , respectively. The MST search applied to NF B gave three close clusters of which only one has a remarkably high  $M$ . We therefore cannot exclude that the cluster is originated by a photon density fluctuation in a region dominated by a high diffuse emission or if it is produced by the superposition of the peripheral radiation of some sources.

**MST(83.955,  $-66.051$ ).** This cluster is one of the most stable features in our NF analysis: a cluster at the same position is, in fact, found for different choices of the selection parameters, energy ranges and searching regions. It is clearly associated with SNR N 63A as was already discussed in Paper I. The photon map showing the cluster associated with this object is also shown in Figure 3.

**MST(84.278,  $-69.160$ ).** As already found in Paper I, this cluster is the richest and the densest one in the sample. It has a correspondent source in the 4FGL-DR2 (P2 source), safely associated with the SNR N 157B: the angular separation between the cluster centroid and the remnant is  $3.5'$ , lower than in Paper I and well compatible with instrumental PSF at these energies. However, the large value of maximum radius, close to  $25'$ , much higher than the X-ray size of the PWN, which according to Wang et al. (2001) is around  $0.5'$ , suggests the presence of an extended component. The analysis performed applying  $\Lambda_{\text{cut}} = 0.5$  gives an even denser cluster with only a slightly lower photon number and  $R_{\text{max}} = 19.4'$ . These results confirm the this feature is embedded in an extended emission, as already reported in Paper I.

**MST(85.186,  $-69.329$ ).** A similar feature was already reported in Paper I. It corresponds to another one of the four sources detected by Ackermann et al. (2016) and its counterpart is SNR B0540-693 with the young pulsar PSR J0540-6919. This source is located in one of the brightest regions and for this reason it is not included in the list of clusters detected above 6 GeV, since it is unresolved from the near extended cluster which has a radius of about  $38'$ . It is detected in NF B, but with a variable  $M$ , depending on the adopted  $\Lambda_{\text{cut}}$ : with a separation length equal to 0.6 the corresponding cluster has 20 photons and  $M = 59.217$ , while for  $\Lambda_{\text{cut}} = 0.7$  these values are reduced to 8 photons and  $M = 18.035$ . For this reason one cannot consider this a VS cluster, but its very high magnitudes in some searches correspond to a very significant feature.

**MST(90.281,  $-70.568$ ).** This rich cluster corresponds to a source in the 4FGL-DR2 catalogue. It is outside of all considered NFs. It was already found in Paper I as a high significance cluster, clearly associated with the background flat spectrum radio quasar 5BZQ J0601-7036 (PKS 0601-70).

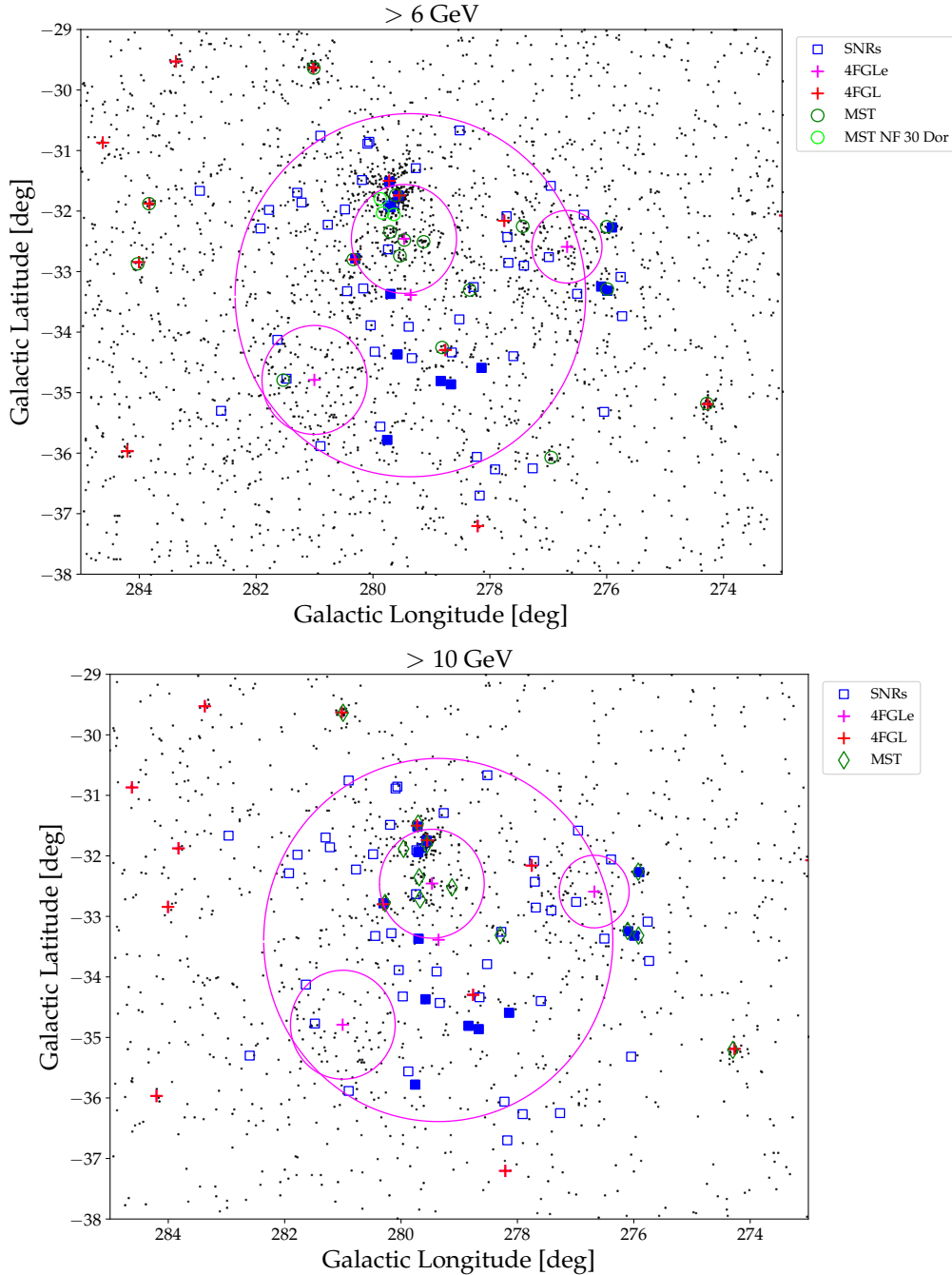


**Figure 2.** Upper panel: Photon map in Galactic coordinates of the sky region at energies higher than 6 GeV. Red and magenta crosses mark the positions of 4FGL-DR2 sources (point-like and extended), magenta circles are the sizes of the extended ones; blue squares are the SNRs in the Maggi et al. (2016) catalogue and filled squares are those with an X-ray luminosity higher than  $10^{36}$  erg/s; dark green circles are MST clusters found in the analysis at energy higher than 6 GeV and  $\Lambda_{\text{cut}} = 0.7$  undetected above 10 GeV; light green circles are the clusters found in the region of 30 Doradus complex. Lower panel: Photon map in Galactic coordinates of the sky region at energies higher than 10 GeV. Source symbols are as in the upper panel; green diamonds are the clusters found in the large field analysis at energies higher than 10 GeV and  $\Lambda_{\text{cut}} = 0.7$ .

### 3.2 Details on individual clusters at energies > 6 GeV

In the following we report the main properties of only the clusters not found above 10 GeV.

**MST(74.306, -66.225).** It is the cluster with the highest  $M$  in this sample; it is found above 8 GeV but not above 10 GeV, that could imply a rather soft spectrum with a cut-off around this energy. Its

position is rather peripheral and does not correspond to any known SNR. The search for a possible counterpart indicates at a rather short angular separation a SUMSS radio source with an optical  $B$  magnitude around 20.0, corresponding also to a ROSAT X-ray source. It might be associated with a background blazar, but further observations are necessary to confirm its nature.

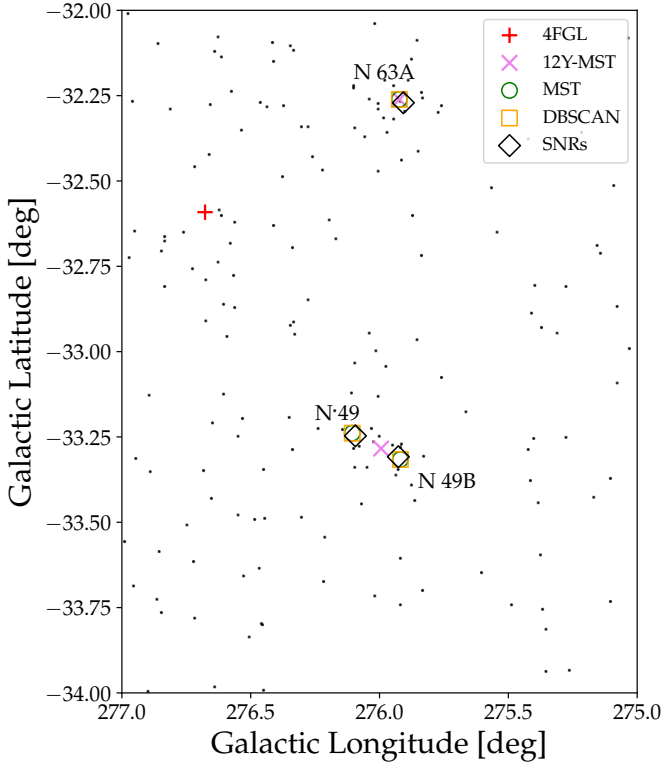


**Figure 3.** Photon map in Galactic coordinates of the sky region including the SNRs N 63A, N 49 and N 49B at energies higher than 6 GeV. Open diamonds are the SNRs, large violet crosses are the clusters in the 12Y-MST catalogue, green circles are the MST clusters found in the present analysis as reported in Table 1 above 10 GeV, while orange squares are the DBSCAN clusters reported in in Table 2. The red cross is only source in the 4FGL-DR2 catalogue detected in this region.

**MST(74.875, -70.169).** This cluster with a high  $M$  value above 6 GeV is located at a rather short angular separation from the SNR N 186D, well compatible with the angular resolution at these energies. In the large field analysis there is a cluster with only 4 photons and  $M \approx 15$ . It is located in the same area covered by the LMC-FarWest. The association with the SNR N 186D appears likely although not firmly established.

**MST(77.934, -68.137).** This cluster is in the large field analysis with a value of  $M$  just below the adopted threshold. It has a clear correspondence with a 4FGL-DR2 source, associated in this catalogue with a background AGN of uncertain classification. There is a faint SNR in the Maggi et al. (2016) list at the angular distance of  $5'8$ , slightly higher than  $R_{\max}$ . We can consider this detection as safely established, while its nature is not well understood.

**MST(78.936, -72.681).** There is a very well positional correspondence with a 4FGL-DR2 source whose candidate counterpart is a flat spectrum radio source (PKS 0517–726) classified as a blazar of uncertain type (see also D’Abrusco et al. 2019). A  $\gamma$ -ray flare with a rather hard spectrum was reported in December 2018 (Rani et al. 2018). Considering that it is undetected above 10 GeV, while a low  $M$  cluster is found at energies higher than 8 GeV, one can expect the occurrence of a sharp cutoff around this energy.

**MST(82.317, -72.740).** Its coordinates are very close to those of a 4FGL-DR2 associated with the flat spectrum radio source (PKS 0530–727) classified as a blazar of a mixed type between BL Lacs and flat spectrum radio quasars (D’Abrusco et al. 2019). A cluster with  $M = 17.803$  is found at energies higher than 8 GeV, while no feature is found in the MST search above 10 GeV.

**MST(83.643, -67.326).** This is a rather rich cluster without any corresponding feature at energies higher than 8 GeV. In the NF analysis it is divided into a couple of near clusters which are joined together when a slightly higher  $\Lambda_{\text{cut}} = 0.8$  is chosen; again, no feature is found at higher energies. The cluster is not very stable and its detection is critically dependent on the selection parameters. Likely it could be originated by local density fluctuations in a relatively bright region.

### 3.3 A new cluster from NF analyses

Complementary cluster NF searches to verify and to extend the results above 10 GeV, provided only a new cluster having a magnitude higher than 20, indicated as MST(83.553, -69.203) using the same nomenclature as before. At energies higher than 6 GeV, this cluster has only 6 photons but a quite high  $g = 3.944$  that implies a magnitude  $M = 23.655$ . At higher energies no significant cluster is found. It is well embedded in the 30 Dor complex and consequently its significance cannot be safely established, because it is not easy to exclude a local background fluctuation. A tentative analysis down to 4 GeV gave clusters with a well compatible position but a magnitude critically dependent on  $\Lambda_{\text{cut}}$ . Moreover, its angular distance from SN 1987A is about  $23'$ , large enough for a possible association.

In any case we searched for some possible interesting candidate counterpart and found a radio (PMN J0536–6909) and X-ray source (2XMM J053438.1–691003) at an angular separation lower than  $3'$ , whose nature is not known.

## 4 BRIGHT SNRS IN LMC

In Table 1 some of the reported detections correspond to SNRs with high X-ray luminosity. We then extracted from the Maggi et al. (2016) list a subsample of 13 bright sources having a luminosity higher than  $10^{36} \text{ erg s}^{-1}$ . Six remnants of this subsample were found associated with significant clusters, as discussed in the previous sections. In the same table we reported also the flux densities at 1 GHz from the Bozzetto et al. (2017) catalogue: 12 sources (20%) of 59 confirmed SNRs are above this value, and only 5 (about 10%) have a flux density higher than 1 Jy. All these radio bright remnants are detected in our analysis and only N 49B has a flux density lower than 1.0 Jy. In the third section of this Table we reported the other four SNRs belonging to the subset of radio flux density higher than 0.5 Jy, which have a much older age estimates and rather low X-ray luminosity. No correlation is found between the radio and  $\gamma$ -ray fluxes (the linear correlation coefficient is 0.07), however, these results suggest that the total energy output of the detected SNRs is remarkably higher than that of other sources. We then investigated in more detail if some of the remaining remnants, reported in Table 3, may be found among the low significance clusters, in energy ranges higher than 6 GeV. In particular we applied MST to small fields of  $2^\circ \times 2^\circ$  approximately centred on the various remnants and no interesting cluster was found near the coordinates of these remnants. We can conclude that, if these sources are gamma-ray loud, their spectrum should have a cut-off at energies lower than 6 GeV.

#### 4.1 Evaluation of $\gamma$ -ray fluxes

Given the very complex background structure in the LMC, to extract the  $\gamma$ -ray fluxes from the selected source candidates using the standard ML is rather difficult, since this method is extremely sensitive to the spectral model and adopted background structure.

We opted, therefore, to perform a simplified estimate of the  $\gamma$ -ray flux using the aperture photometry method<sup>2</sup>, in which the flux is computed by essentially dividing the photon number in a region of interest by the exposure in same region. For each source in Table 3 which corresponds to a MST cluster, the  $\gamma$ -ray flux has been estimated in the 3–300 GeV band, using as a source region of interest a circle of radius  $0.9R_{\max}$ . The background has been estimated in a circular region of radius  $1.5R_{\max}$  likewise centred on the MST coordinates. Net source fluxes are therefore computed by rescaling and subtracting the expected background. It should be emphasised that a cross-contamination between source and background cannot be excluded, but the resulting estimate should be a reliable indication of the actual  $\gamma$ -ray flux. The last column in Table 3 reports the evaluated fluxes. This simple method cannot be safely applied at energies below a few GeV because the radius of the PSF is larger and the evaluation of the local background is much more uncertain. A preliminary study of the diffuse emission in LMC is necessary. For the same reason, reliable estimates of  $\gamma$ -ray spectral indices cannot be performed. The comparison between the aperture photometric values and those obtained by ML analysis for N 157B (Ackermann et al. 2016) and N 63A (Campana et al. 2018a) are in a satisfactory agreement within the reported standard deviations, with only a possible underestimate not higher than 25%. Thus we conclude that for the previously detected SNRs the fluxes obtained here are consistent with those derived from the standard ML analysis.

## 5 DISCUSSION AND CONCLUSION

The MST and DBSCAN methods applied to the complex region of LMC provides a new evidence for high energy emission from some SNRs. It is well known that this small close galaxy is rich of SNRs concentrated in a sky region of few square degrees. There is also a strong diffuse emission likely originated by a local component of cosmic rays interacting with the interstellar gas of HII regions, in particular in the 30 Dor nebula. This diffuse component can present some local emission fluctuations which make difficult the identification of sources against this non uniform background.

We considered in our analysis photons in the two energy ranges defined by the two lower limits of 6 GeV and 10 GeV, in which the Galactic diffuse emission is low enough to allow a safe extraction of clusters. The analysis was also applied to small regions to verify the stability of selected clusters. Some of these regions exclude 30 Dor to avoid the possibility of a reduced capability to extract genuine features given the high photon density around this source.

The capability of the MST method for extracting clusters in  $\gamma$ -ray images is described in the paper on the recent catalogue of candidate sources at Galactic latitudes higher than  $20^\circ$  (Campana & Massaro 2021). The validity of this approach is confirmed by the present analysis, in which we found high significance clusters corresponding to the sources detected by Ackermann et al. (2016) and also those reported in the 4FGL-DR2 catalogue, with the exception of those with a soft spectrum and consequently a quite low high energy flux.

DBSCAN was already successfully applied to  $\gamma$ -ray cluster detection (Tramacere & Vecchio 2013), and the estimated significance is highly correlated with  $TS$  provided by Fermi-LAT maximum likelihood analysis. The excellent agreement with the results provided by the MST analysis supplies a further validation for the robustness of the detected clusters. The only two clusters detected above 10 GeV, and not present in the MST analysis, result likely from the fragmentation of the source MST(81.700,  $-69.129$ ), as confirmed by the close position and total number of detected photons.

From the results given in Table 1 it is possible to extract a final sample of 20 clusters, of which 11 are present in the two energy ranges: 7 clusters are found above 6 GeV, but not above 10 GeV, and only 2 above 10 GeV. Considering the possible counterparts, 5 clusters might be associated with background blazars, but only one of them is safely confirmed as FSRQ while the nature of the remaining 4 is uncertain; 7 clusters are clearly associated with SNRs, one of which harbouring a pulsar. In Table 3 we listed the 13 brightest SNRs in the explored region, with an X-ray luminosity higher than  $5 \times 10^{36}$  erg s<sup>-1</sup>. Six of them are associated with clusters, and particularly the 4 with the highest luminosity. The only cluster in this bright sample not associated with a SNR is MST(80.630,  $-67.891$ ) whose candidate counterpart is N 44. This remnant has an X-ray luminosity of  $9 \times 10^{34}$  erg s<sup>-1</sup> and is well separated from the near bright 30 Dor region. It is interesting that the cluster at energies higher than 6 GeV has about twice the photons found above 10 GeV, a result confirmed applying a separation length of  $0.6\Lambda_m$  and also by the NF searches. This suggest that it has a rather soft spectrum.

Figure 4 shows the X-ray luminosities (in the 0.3–10 keV band) of the SNRs detected with Fermi-LAT as a function of their  $\gamma$ -ray luminosity in the 1–100 GeV band. Galactic SNRs are indicated by black crosses, the LMC SNRs N 132D, N 63A, B0540-693, N 157B by red crosses, while blue crosses mark N 49 and N 49B (see Appendix A for details).  $\gamma$ -ray fluxes were extrapolated at 1 GeV assuming a photon index  $\Gamma = 2$ , as in the usual prescription of the Fermi-LAT collaboration for data analysis; this value is slightly harder than the mean value of the Galactic SNRs, which according to Acero et al. (2016) is equal to 2.5. The ranges of X-ray and  $\gamma$ -ray luminosity derived for LMC SNRs are nicely consistent with that of Galactic SNRs: in fact, about one third of Galactic remnants emit in the X-ray or  $\gamma$ -ray band with a power comparable to those detected in LMC, though we notice that only five sources are among the brightest remnants in both energy bands. Our new detections indicate that the subsample of SNRs in LMC has energetic properties similar to the Galactic ones, even considering the bias toward high fluxes associated with the distance of the LMC and its large  $\gamma$ -ray background.

### 5.1 Properties of some detected SNRs

In the following we describe the main properties of confirmed or newly detected SNRs in our analysis.

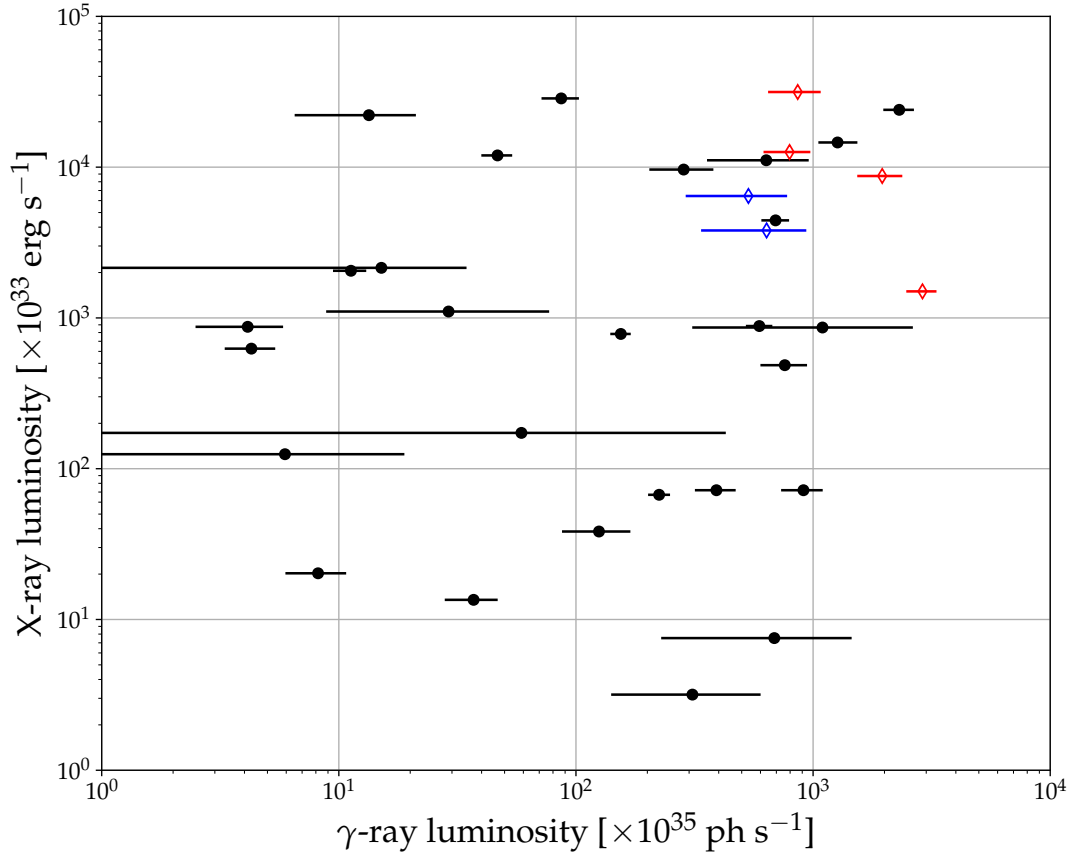
**N 132D.** This is the remnant of a core-collapse SN with an age since explosion of  $\approx 2400$  years (Law et al. 2020). It is the brightest X-ray emitting SNR in LMC (Clark et al. 1982; Hwang et al. 1993; Favata et al. 1997; Borkowski et al. 2007) and its emission in the high energy  $\gamma$ -ray and TeV ranges is firmly established (H. E. S. S. Collaboration et al. 2021; Ackermann et al. 2016). According to the model considerations developed by H. E. S. S. Collaboration et al. (2021), the  $\gamma$ -ray emission exhibits a dominant hadronic component formed by a diffusive shock acceleration. It is possible that the remnant is in interaction with a complex of molecular clouds (e.g., Dopita et al. 2018; Law et al. 2020) partially within the spatial confidence region of the

<sup>2</sup> [https://fermi.gsfc.nasa.gov/ssc/data/analysis/scitools/aperture\\_photometry.html](https://fermi.gsfc.nasa.gov/ssc/data/analysis/scitools/aperture_photometry.html)

**Table 3.** SNRs in the LMC region with a X-ray luminosity in the band 0.3–8 keV higher than  $10^{36}$  erg s $^{-1}$  from the Maggi et al. (2016) list. Radio flux densities at 1 GHz are from Bozzetto et al. (2017).

SNR	MCSNR	X size '	$L_X$ $10^{35}$ erg s $^{-1}$	$S_{1\text{GHz}}$ Jy	Type	Age kyr	MST/DBSCAN detection	$\gamma$ -ray flux* $10^{-11}$ ph cm $^{-2}$ s $^{-1}$	Interaction w/ dense CSM
N 132D	J0525–6938	2.1	315.04	5.26	CC	2.4	yes	$9.2 \pm 2.3$	yes
N 63A	J0535–6602	1.4	126.00	1.86	CC	3.5	yes	$8.5 \pm 1.9$	possible
B0540–693	J0540–6920	1.2	87.35	1.03	CCP	1.14	yes	$20.9 \pm 4.5$	no
N 49	J0526–6605	1.4	64.37	1.66	CC	4.8	yes	$5.7 \pm 2.6^\dagger$	yes
N 49B	J0526–6605	2.8	38.03	0.63	CC	$\sim 10$	yes	$6.8 \pm 3.2^\dagger$	possible
N 157B	J0537–6910	2.0	15.00	2.88	CCP	$\sim 5$	yes	$30.9 \pm 4.5$	yes
SNR1987A	J0535–6916	0.03	27.39	0.82	CC	0.03	confused		yes
B0453-685	J0453–6829	2.0	13.85	0.21	CC	12.0	no		no
N 23	J0505–6802	1.6	26.25	0.39	CC(?)	4.6	no		no
N 103B	J0509–6843	0.5	51.70	0.58	Ia	0.86	no		no
DEM L71	J0505–6753	1.3	44.59	0.01	Ia	4.4	no		no
B0519–690	J0519–6902	0.6	34.94	0.13	Ia	0.6	no		no
B0509–67.5	J0509–6731	0.53	16.51	0.10	Ia	0.4	no		no
B0450-709	J0450–7050	5.67	0.59	0.69	CC(?)	$\sim 70$	no		no
DEM L316B	J0547–6942	3.17	1.47	0.73	CC(?)	40.5	no		yes
DEM L316A	J0547–6941	3.17	1.26	0.52	CC(?)	33.0	no		yes
DEM L328	J0550–6823	5.20	1.22	0.65	CC(?)		no		possible

(\*) Photon flux evaluated in the 3–300 GeV energy band. – ( $^\dagger$ ) Values possibly affected by the nearby SNR. – CC = Core collapse; CCP = Core collapse Plerion


**Figure 4.** Unabsorbed X-ray luminosity of SNRs (0.3–10 keV band) versus the corresponding  $\gamma$ -ray luminosity, as measured by *Fermi*-LAT in the 1–100 GeV band. Luminosities for N 132D, N 63A, B0540-693, N 157B (red diamonds), and for N 49 and N 49B (blue diamonds) were derived from the values reported in Table 3 assuming a photon index  $\Gamma = 2$  and a distance of 51 kpc. See Appendix A for details.

source. The photon flux estimated by means of aperture photometry (see Table 3) is substantially in a good agreement with the one derived from the power-law spectrum with a photon index  $\Gamma = 1.4$  given by [Ackermann et al. \(2016\)](#) that is  $1.2 \times 10^{-10}$  ph cm $^{-2}$  s $^{-1}$  in the same energy range.

**N 63A.** This is a bright core-collapse SNR embedded within the large HII region N63, associated with dense molecular clouds, shock-ionised gas, and photoionised gas. Its age is estimated to be about 3500 years ([Sano et al. 2019](#)) or within the range 2000 – 5000 yr (e.g., [Hughes et al. 1998](#); [Warren et al. 2003](#)). This source is the second brightest SNR in LMC and was observed from radio to X-rays ([Warren et al. 2003](#); [Williams et al. 2006a](#); [Caulet & Williams 2012](#); [Sano et al. 2019](#)). Its estimated X-ray luminosity is  $4 \times 10^{34}$  ergs s $^{-1}$ , probably due to an embedded PWN ([Warren et al. 2003](#)). The first detection of a  $\gamma$ -ray emission from this bright SNR was already reported in Paper I and was validated by the ML analysis, with  $\sqrt{TS} = 9$  and a flux above 1 GeV equal to  $(3.4 \pm 0.6) \times 10^{-10}$  ph cm $^{-2}$  s $^{-1}$ . It is located in near the border of the central high density region of LMC (see Figure 2) and therefore it is not highly affected by background fluctuations. [Sano et al. \(2019\)](#) assumed that the  $\gamma$ -ray emission is dominated by hadronic component and estimated the total energy output in cosmic-ray protons and the magnetic field which resulted roughly consistent with the Galactic SNRs.

**B0540–693.** This is a composite high luminosity remnant of a core-collapse SN that exhibits a segmented shell emission with an inner bright PWN (PSR J0540–6919). Its estimated age is 1140 years ([Williams et al. 2008](#)). The X-ray emission structure originates from two “arcs” near the E and W boundaries and the spectral distribution implies a synchrotron origin ([Park et al. 2010](#); [McEntaffer et al. 2012](#)) from electrons accelerated in the supernova shock. There is no evidence of interaction of the remnant with dense clouds of the ISM. We argue that the high level of  $\gamma$ -ray emission detected may originate from the PWN.

**N 49.** Another bright remnant of a core-collapse SN, among the brightest SNRs in LMC. Its estimated age is 4800 years (e.g., [Park et al. 2012a](#)). A magnetar (SGR B0526–66) is clearly detectable as a bright point-like X-ray source ([Park et al. 2012b](#); [Zhou et al. 2019](#)) closer to the North boundary than to the centre. The magnetar has been recently detected by NuSTAR ([Park et al. 2020](#)) in a quiescent state up to 40 keV; above about 10 keV the emission is dominated by a power-law component. The physical association of the magnetar and the SNR, however, is not yet safely established, and the possibility of a casual spatial coincidence cannot be ruled out. We do not know if this magnetar exhibits or not a quiescent emission in the high energy  $\gamma$ -rays, but no detection in the TeV range has been reported up to now ([Komin et al. 2019](#)). Multi-wavelengths observations show clear evidence of interaction of the remnant with dense clumpy interstellar clouds on the eastern side of the remnant ([Vancura et al. 1992](#); [Banias et al. 1997](#)). The interaction leads to bright emission in radio, optical, infrared, ultraviolet, and X-ray bands (e.g., [Park et al. 2003](#); [Sankrit et al. 2004](#); [Williams et al. 2006b](#); [Rakowski et al. 2007](#); [Bilikova et al. 2007](#); [Otsuka et al. 2010](#); [Park et al. 2012a](#)).

**N 49B.** This remnant is a core-collapse SNR with an estimated dynamical age of  $\approx 10000$  years ([Hughes et al. 1998](#)). Its X-ray structure was investigated by [Park & Bhalerao \(2017\)](#) who supported the possibility of a large mass progenitor. The X-ray luminosity of this SNR, however, is about the 60% of that of N 49; in any case it is certainly among the brightest remnants in the LMC. The angular

separation between N 49 and N 49B is comparable with the  $\gamma$ -ray resolution at energies of  $\approx 10$  GeV or higher but they cannot be resolved at lower energies. Nevertheless, the elongation of the cluster in the direction connecting the two SNRs is an indication that both are responsible for the detected feature. [Chu & Kennicutt \(1988\)](#) evidenced a close proximity of N 49B with the HII region DEM 181 and a possible association with a molecular cloud (see, also, [Cohen et al. 1988](#)). In particular, the superposition of faint and bright features suggests that the remnant is expanding through a cloudy ISM. In light of this, [Chu & Kennicutt \(1988\)](#) suggested a Population I progenitor for N49B.

**N 157B.** This is the remnant of a core-collapse SN, characterized by a large physical size in both radio and X-ray bands (e.g., [Wang & Gotthelf 1998](#); [Lazendic et al. 2000](#)). Its age is not well constrained; however, according to the average ionization age inferred from the analysis of X-ray observations, the estimated age of the remnant could be  $\approx 5000$  years ([Chen et al. 2006](#)). The remnant contains the young pulsar PSR J0537–6910, an ultrafast X-ray pulsar with a period of 16 ms, surrounded by a X-ray–bright nonthermal PWN ([Marshall et al. 1998b](#)). The remnant appears to expand through the hot low-density medium of a surrounding superbubbles formed by the young OB association LH 99 ([Lucke & Hodge 1970](#); [Chu et al. 1992](#)); this may explain the unusual large size of the remnant. On the other hand, the comparison between optical and X-ray observations revealed that the explosion site is located close to a dense cloud which led to a reflection shock that is now interacting with the PWN ([Chen et al. 2006](#)).

**N 44.** This is the only candidate counterpart of clusters that is not directly associated with a SNR. In fact, N 44 is a rather complex nebula identified as an active star forming region with superbubble structure, comprising a large complex of H II regions ([Kennicutt & Hodge 1986](#); [Pellegrini et al. 2012](#); [Ksoll et al. 2021](#)). The nebula is populated by three OB associations (LH47, 48 and 49; [Lucke & Hodge 1970](#)) and several massive O-type stars (see [Ksoll et al. 2021](#) and references therein). Interestingly, N 44 also hosts SNR 0523-679 ([Chu et al. 1993](#)), a remnant showing a high  $\alpha$ /Fe ratio as expected from core-collapse SNe and with a total X-ray luminosity of  $5.73 \times 10^{35}$  ergs s $^{-1}$  ([Jaskot et al. 2011](#)). Given the complexity of the region and the wealth of high-energy objects in N 44, we cannot identify the object mainly responsible for the detected cluster.

We note that the SNRs associated with our detected clusters are all remnants of core-collapse SNe and the vast majority of them show clear evidence of interaction with a dense ambient medium. The only exception is B0540–693 which, however, hosts the young and energetic pulsar PSR J0540–6919 which may be responsible for the intense  $\gamma$ -ray emission. All other SNRs in Table 3 cannot be uniquely associated with any of our clusters. Of these, the very young remnant of the core-collapse SN 1987A is the only one for which a strong interaction with a highly structured CSM (consisting of an HII region and a dense ring) is known. This remnant, however, was not considered as a possible counterpart of our clusters, as it is located in a very complex and rich area, so a unique association is not possible. Furthermore, [Sano et al. \(2018\)](#) suggested that the SN originating N 103B exploded in a bubble driven by the accretion wind from the progenitor system. Thus, N 103B is now interacting with the dense gas wall and the observations show evidence of strong interaction between the SN ejecta and the dense CSM ([Yamaguchi et al. 2014](#)). Indeed all other remnants show no evidence of interaction with a dense CSM. We also note that most of these remnants originate from

Type Ia SNe (N 103B, DEM L71, B0519–690, B0509–67.5), with the exception of N 23 (for which, however, there is no consensus for its type of explosion, a core-collapse or Ia; Hayato et al. 2006) and B0453–685 (a fairly old SNR with an age of  $\approx 12000$  years, which propagates through a low-density medium and shows an almost circular shape with no hints of interaction with clouds; Haberl et al. 2012). More detailed observational analyses would be useful for improving the knowledge of the high energy emission from these objects, in particular for comparing their spectral distribution in different frequency bands. However, in the light of available information, we can conclude that the counterparts of our clusters are only core-collapse SNRs mostly interacting with a dense medium. This evidence may indicate a hadronic origin for their  $\gamma$ -ray emission.

## ACKNOWLEDGMENTS

We are grateful to the referee D. Urošević for his useful comments. We acknowledge use of archival Fermi data. F.B., M.M. and S.O. acknowledge financial contribution from the PRIN INAF 2019 grant “From massive stars to supernovae and supernova remnants: driving mass, energy and cosmic rays in our Galaxy”.

## DATA AVAILABILITY

Data used in this paper are available on request.

## REFERENCES

- Abdo A. A., et al., 2010, *A&A*, **512**, A7
- Abdollahi S., et al., 2020, *ApJS*, **247**, 33
- Acero F., Ballet J., Decourchelle A., Lemoine-Goumard M., Ortega M., Giacani E., Dubner G., Cassam-Chenaï G., 2009, *A&A*, **505**, 157
- Acero F., et al., 2016, *ApJS*, **224**, 8
- Acero F., Lemoine-Goumard M., Ballet J., 2022, arXiv e-prints, p. [arXiv:2201.05567](https://arxiv.org/abs/2201.05567)
- Ackermann M., et al., 2012, *ApJS*, **203**, 4
- Ackermann M., et al., 2013a, *Science*, **339**, 807
- Ackermann M., et al., 2013b, *ApJ*, **765**, 54
- Ackermann M., et al., 2016, *A&A*, **586**, A71
- Ajello M., et al., 2017, *ApJS*, **232**, 18
- Ballet J., Burnett T. H., Digel S. W., Lott B., 2020, arXiv e-prints, p. [arXiv:2005.11208](https://arxiv.org/abs/2005.11208)
- Bamba A., Yamazaki R., Ueno M., Koyama K., 2003, *ApJ*, **589**, 827
- Bamba A., Sawada M., Nakano Y., Terada Y., Hewitt J., Petre R., Angelini L., 2016, *PASJ*, **68**, S5
- Banas K. R., Hughes J. P., Bronfman L., Nyman L. Å., 1997, *ApJ*, **480**, 607
- Bell A. R., 2004, *MNRAS*, **353**, 550
- Bell A. R., Schure K. M., Reville B., Giacinti G., 2013, *MNRAS*, **431**, 415
- Bernieri E., Campana R., Massaro E., Paggi A., Tramacere A., 2013, *A&A*, **551**, L5
- Bilikova J., Williams R. N. M., Chu Y. H., Gruendl R. A., Lundgren B. F., 2007, *AJ*, **134**, 2308
- Borkowski K. J., Hendrick S. P., Reynolds S. P., 2007, *ApJ*, **671**, L45
- Bozzetto L. M., et al., 2017, *ApJS*, **230**, 2
- Campana R., Massaro E., 2021, *A&A*, **652**, A6
- Campana R., Massaro E., Gasparrini D., Cutini S., Tramacere A., 2008, *MNRAS*, **383**, 1166
- Campana R., Bernieri E., Massaro E., Tinebra F., Tosti G., 2013, *Ap&SS*, **347**, 169
- Campana R., Massaro E., Bernieri E., D’Amato Q., 2015, *Ap&SS*, **360**, 19
- Campana R., Massaro E., Bernieri E., 2016a, *Ap&SS*, **361**, 183
- Campana R., Massaro E., Bernieri E., 2016b, *Ap&SS*, **361**, 185
- Campana R., Massaro E., Bernieri E., 2016c, *Ap&SS*, **361**, 367
- Campana R., Maselli A., Bernieri E., Massaro E., 2017, *MNRAS*, **465**, 2784
- Campana R., Massaro E., Bernieri E., 2018a, *Ap&SS*, **363**, 144
- Campana R., Massaro E., Bernieri E., 2018b, *A&A*, **619**, A23
- Caulet A., Williams R. M., 2012, *The Astrophysical Journal*, **761**, 107
- Chen Y., Wang Q. D., Gotthelf E. V., Jiang B., Chu Y.-H., Gruendl R., 2006, *ApJ*, **651**, 237
- Chu Y.-H., Kennicutt Robert C. J., 1988, *AJ*, **96**, 1874
- Chu Y.-H., Kennicutt Robert C. J., Schommer R. A., Laff J., 1992, *AJ*, **103**, 1545
- Chu Y.-H., Mac Low M.-M., Garcia-Segura G., Wakker B., Kennicutt Robert C. J., 1993, *ApJ*, **414**, 213
- Clark D. H., Tuohy I. R., Dopita M. A., Mathewson D. S., Long K. S., Szymkowiak A. E., Culhane J. L., 1982, *ApJ*, **255**, 440
- Cline T. L., et al., 1982, *ApJ*, **255**, L45
- Cohen R. S., Dame T. M., Garay G., Montani J., Rubio M., Thaddeus P., 1988, *ApJ*, **331**, L95
- Corbet R. H. D., et al., 2016, *ApJ*, **829**, 105
- Cormen T., Leiserson C., Rivest R., Stein C., 2009, Introduction to Algorithms, 3rd edn. MIT Press, Cambridge, USA
- Cusumano G., Maccarone M. C., Mineo T., Sacco B., Massaro E., Bandiera R., Salvati M., 1998, *A&A*, **333**, L55
- D’Abrusco R., et al., 2019, *ApJS*, **242**, 4
- Dopita M. A., Vogt F. P. A., Sutherland R. S., Seitzzahl I. R., Ruiter A. J., Ghavamian P., 2018, *ApJS*, **237**, 10
- Dubner G., Loiseau N., Rodríguez-Pascual P., Smith M. J. S., Giacani E., Castelletti G., 2013, *A&A*, **555**, A9
- Easter M., Kriegel H., Sander J., Xu X., 1996, In Proceedings of the 2nd International Conference on Knowledge Discovery and Data Mining
- Favata F., Vink J., Parmar A. N., Kaastra J. S., Mineo T., 1997, *A&A*, **324**, L45
- Finley J. P., Oegelman H., 1994, *ApJ*, **434**, L25
- Gabici S., 2017, in 6th International Symposium on High Energy Gamma-Ray Astronomy. p. 020002 ([arXiv:1610.06234](https://arxiv.org/abs/1610.06234)), doi:10.1063/1.4968887
- Gaensler B. M., Fogel J. K. J., Slane P. O., Miller J. M., Wijnands R., Eikenberry S. S., Lewin W. H. G., 2003, *ApJ*, **594**, L35
- Ginzburg V. L., 1972, *Nature Physical Science*, **239**, 8
- Ginzburg V. L., Ptuskin V. S., 1984, *Journal of Astrophysics and Astronomy*, **5**, 99
- Giordano F., et al., 2012, *ApJ*, **744**, L2
- Green D. A., 2019, *Journal of Astrophysics and Astronomy*, **40**, 36
- H. E. S. S. Collaboration et al., 2021, *A&A*, **655**, A7
- H.E.S.S. Collaboration et al., 2012, *A&A*, **545**, L2
- H.E.S.S. Collaboration et al., 2015, *Science*, **347**, 406
- Haberl F., et al., 2012, *A&A*, **543**, A154
- Harris I., Smith R., Slane P., Hughes J., 2006, in Wilson A., ed., ESA Special Publication Vol. 604, The X-ray Universe 2005. p. 369
- Hayato A., Bamba A., Tamagawa T., Kawabata K., 2006, *ApJ*, **653**, 280
- Hillas A. M., 2005, *Journal of Physics G Nuclear Physics*, **31**, R95
- Hughes J. P., Hayashi I., Koyama K., 1998, *ApJ*, **505**, 732
- Hwang U., Hughes J. P., Canizares C. R., Markert T. H., 1993, *ApJ*, **414**, 219
- Jaskot A. E., Strickland D. K., Oey M. S., Chu Y. H., García-Segura G., 2011, *ApJ*, **729**, 28
- Jolliffe I. T., 1986, Principal component analysis. <http://adsabs.harvard.edu/abs/1986pca...book.....J>
- Kennicutt R. C. J., Hodge P. W., 1986, *ApJ*, **306**, 130
- Komin N., Haupt M., H. E. S. S. Collaboration 2019, in 36th International Cosmic Ray Conference (ICRC2019). p. 716 ([arXiv:1908.04656](https://arxiv.org/abs/1908.04656))
- Koo B.-C., Kim K.-T., Seward F. D., 1995, *ApJ*, **447**, 211
- Koyama K., Petre R., Gotthelf E. V., Hwang U., Matsuura M., Ozaki M., Holt S. S., 1995, *Nature*, **378**, 255
- Ksoll V. F., et al., 2021, *AJ*, **161**, 257
- Ku W. H. M., Kahn S. M., Pisarski R., Long K. S., 1984, *ApJ*, **278**, 615
- Law C. J., et al., 2020, *ApJ*, **894**, 73
- Lazendic J. S., Dickel J. R., Haynes R. F., Jones P. A., White G. L., 2000, *ApJ*, **540**, 808
- Lazendic J. S., Slane P. O., Hughes J. P., Chen Y., Dame T. M., 2005, *ApJ*, **618**, 733
- Leahy D. A., Aschenbach B., 1996, *A&A*, **315**, 260

Leahy D. A., Naranan S., Singh K. P., 1986, *MNRAS*, **220**, 501  
 Leahy D. A., Green K., Ranasinghe S., 2013, *MNRAS*, **436**, 968  
 Li T.-P., Ma Y.-Q., 1983, *Astrophysical Journal*, **272**, 317  
 Lucke P. B., Hodge P. W., 1970, *AJ*, **75**, 171  
 Maggi P., et al., 2016, *A&A*, **585**, A162  
 Marshall F. E., Gotthelf E. V., Zhang W., Middleditch J., Wang Q. D., 1998a, *ApJ*, **499**, L179  
 Marshall F. E., Gotthelf E. V., Zhang W., Middleditch J., Wang Q. D., 1998b, *ApJ*, **499**, L179  
 Matsui Y., Long K. S., Tuohy I. R., 1988, *ApJ*, **329**, 838  
 Mattox J. R., et al., 1996, *ApJ*, **461**, 396  
 Mazets S. E., et al., 1979a, *Soviet Astronomy Letters*, **5**, 166  
 Mazets E. P., Golentskii S. V., Ilinskii V. N., Aptekar R. L., Guryan I. A., 1979b, *Nature*, **282**, 587  
 McEntaffer R. L., Brantseg T., Presley M., 2012, *ApJ*, **756**, 17  
 Miceli M., Decourchelle A., Ballet J., Bocchino F., Hughes J. P., Hwang U., Petre R., 2006, *A&A*, **453**, 567  
 Otsuka M., et al., 2010, *A&A*, **518**, L139  
 Park S., Bhalerao J., 2017, *ApJ*, **834**, 189  
 Park S., Burrows D. N., Garmire G. P., Nousek J. A., Hughes J. P., Williams R. M., 2003, *ApJ*, **586**, 210  
 Park S., Hughes J. P., Slane P. O., Mori K., Burrows D. N., 2010, *ApJ*, **710**, 948  
 Park S., Hughes J. P., Slane P. O., Burrows D. N., Lee J.-J., Mori K., 2012a, *ApJ*, **748**, 117  
 Park S., Hughes J. P., Slane P. O., Burrows D. N., Lee J.-J., Mori K., 2012b, *ApJ*, **748**, 117  
 Park S., Bhalerao J., Kargaltsev O., Slane P. O., 2020, *ApJ*, **894**, 17  
 Pellegrini E. W., Oey M. S., Winkler P. F., Points S. D., Smith R. C., Jaskot A. E., Zastrow J., 2012, *ApJ*, **755**, 40  
 Petriella A., Paron S. A., Giacani E. B., 2013, *A&A*, **554**, A73  
 Ptuskin V. S., Zirakashvili V. N., 2005, *A&A*, **429**, 755  
 Rakowski C. E., Raymond J. C., Szentgyorgyi A. H., 2007, *ApJ*, **655**, 885  
 Rani B., Kreter M., Cheung C. C., 2018, *The Astronomer's Telegram*, **12333**, 1  
 Rho J., Borkowski K. J., 2002, *ApJ*, **575**, 201  
 Rho J., Petre R., 1997, *ApJ*, **484**, 828  
 Ruiz-Lapuente P., 2004, *ApJ*, **612**, 357  
 Sankrit R., Blair W. P., Raymond J. C., 2004, *AJ*, **128**, 1615  
 Sankrit R., Raymond J. C., Blair W. P., Long K. S., Williams B. J., Borkowski K. J., Patnaude D. J., Reynolds S. P., 2016, *ApJ*, **817**, 36  
 Sano H., et al., 2018, *ApJ*, **867**, 7  
 Sano H., et al., 2019, *ApJ*, **873**, 40  
 Sezer A., Gök F., Hudaverdi M., Ercan E. N., 2011, *MNRAS*, **417**, 1387  
 Slane P., et al., 2012, *ApJ*, **749**, 131  
 Sreekumar P., et al., 1992, *ApJ*, **400**, L67  
 Takeda S., Bamba A., Terada Y., Tashiro M. S., Yamazaki R., Ohira Y., Iwakiri W., 2016, *PASJ*, **68**, S10  
 Tang Q.-W., 2018, *Astrophysics and Space Science*, **363**, 25  
 Temim T., Slane P., Castro D., Plucinsky P. P., Gelfand J., Dickel J. R., 2013, *ApJ*, **768**, 61  
 Tian W. W., Li Z., Leahy D. A., Wang Q. D., 2007, *ApJ*, **657**, L25  
 Tramacere A., Vecchio C., 2013, *A&A*, **549**, A138  
 Tramacere A., Paraficz D., Dubath P., Kneib J. P., Courbin F., 2016, *MNRAS*, **463**, 2939  
 Troja E., Bocchino F., Reale F., 2006, *ApJ*, **649**, 258  
 Vancura O., Blair W. P., Long K. S., Raymond J. C., 1992, *ApJ*, **394**, 158  
 Vink J., Laming J. M., 2003, *ApJ*, **584**, 758  
 Wang Q. D., Gotthelf E. V., 1998, *ApJ*, **494**, 623  
 Wang Q. D., Gotthelf E. V., Chu Y.-H., Dickel J. R., 2001, *ApJ*, **559**, 275  
 Warren J. S., Hughes J. P., Slane P. O., 2003, *The Astrophysical Journal*, **583**, 260  
 Williams R. M., Chu Y. H., Gruendl R., 2006a, *Astronomical Journal*, **132**, 1877  
 Williams R. M., Chu Y. H., Gruendl R., 2006b, *AJ*, **132**, 1877  
 Williams B. J., et al., 2008, *ApJ*, **687**, 1054  
 Xiang Y., Jiang Z., 2021, *ApJ*, **908**, 22  
 Yamaguchi H., et al., 2014, *ApJ*, **785**, L27

Yew M., et al., 2021, *MNRAS*, **500**, 2336  
 Zhou P., Vink J., Safi-Harb S., Miceli M., 2019, *A&A*, **629**, A51

## APPENDIX A: X-RAY VS $\gamma$ -RAY LUMINOSITY OF SNRS

The luminosities of Galactic SNRs in the 1–100 GeV band in Figure 4 are derived from the fluxes reported by Acero et al. (2016), except for Kepler's SNR (Xiang & Jiang 2021, but see also Acero et al. 2022) and Tycho's SNRs (Giordano et al. 2012). Unabsorbed X-ray luminosities were derived from the fluxes reported in the Chandra SNR catalog ([https://hea-www.harvard.edu/ChandraSNR/snrcat\\_gal.html](https://hea-www.harvard.edu/ChandraSNR/snrcat_gal.html)), except for W28 (Rho & Borkowski 2002), W30 (Finley & Oegelman 1994), G20.0-00.2 (Petriella et al. 2013), W41 (Tian et al. 2007), W44 (Harris et al. 2006), W49B (Miceli et al. 2006), W51C (Koo et al. 1995), Cygnus Loop (Ku et al. 1984), G78.2+2.1 (Leahy et al. 2013), HB21 (Leahy & Aschenbach 1996), CTB 109 (Rho & Petre 1997), IC 443 (Troja et al. 2006), Monoceros (Leahy et al. 1986), Puppis A (Dubner et al. 2013), Vela Jr. (Takeda et al. 2016), MSH 11-62 (Slane et al. 2012), PKS 1209-52 (Matsui et al. 1988), G298.6-0.0 (Bamba et al. 2016), MSH 15-56 (Temim et al. 2013), RX J1713.7-3946 (Acero et al. 2009), CTB 37A (Sezer et al. 2011), G349.7+0.2 (Lazendic et al. 2005), G357.7-00.1 (Gaensler et al. 2003). To convert fluxes in luminosities, we adopt the distances presented in Acero et al. (2016), except for G020.0-00.2 and G024.7+00.6 (Green 2019 and references therein), G298.6-00.0 (Bamba et al. 2016), Tycho's SNR (Ruiz-Lapuente 2004), and Kepler's SNR (Sankrit et al. 2016).

This paper has been typeset from a  $\text{\TeX}/\text{\LaTeX}$  file prepared by the author.